PHYSICAL REVIEW C VOLUME 59, NUMBER 6 JUNE 1999

Inclusive measurements of the $pp \rightarrow pn\pi^+$ reaction at 420 and 500 MeV

R. G. Pleydon,* W. R. Falk, and M. Benjamintz[†]
Department of Physics, University of Manitoba, Winnipeg, Manitoba, Canada R3T 2N2

S. Yen, P. L. Walden, R. Abegg,[‡] D. Hutcheon, and C. A. Miller
TRIUMF, 4004 Wesbrook Mall, Vancouver, British Columbia, Canada V6T 2A3

M. Hartig
Institut fuer Kernphysik, Universität Münster, D-48149 Münster, Germany

K. Hicks
Department of Physics, Ohio University, Athens, Ohio 45701

G. V. O'Rielly[§]
Department of Physics, University of Northern British Columbia, Prince George, British Columbia, Canada V2N 4Z9

R. Shyam
Saha Institute of Nuclear Physics, 1/AF Bidhan Nagar, Calcutta 700064, India

(Received 7 October 1998)

Inclusive measurements of the pion differential cross sections and analyzing powers have been carried out for the $pp \rightarrow pn\pi^+$ reaction at 420 and 500 MeV using the SASP spectrometer at TRIUMF. Pion energies from the onset of the continuum down to about 25 MeV were covered in the angular range from 23° to 100° (lab). Total cross sections of 0.750 ± 0.075 mb and 2.77 ± 0.28 mb were determined for the $pp \rightarrow pn\pi^+$ reaction at 420 and 500 MeV, respectively. The experimental results are presented and discussed within the framework of a partial wave analysis. Theoretical predictions from a covariant one-boson-exchange model that includes final state interactions, provide a good description of the data. The pion spectra, in the region corresponding to low relative np energies, are also well described by a final state interaction model that uses the $pp \rightarrow d\pi^+$ cross sections as input. Details of the determination of the background corrections and detector efficiencies will be discussed. [S0556-2813(99)03606-7]

PACS number(s): 25.10.+s, 21.45.+v, 24.70.+s

I. INTRODUCTION

The fundamental pion production reactions $NN \rightarrow NN\pi$ have been much studied at intermediate energies since the meson factories came into operation nearly thirty years ago. These reactions play central roles in the nucleon-nucleon interaction and in the interaction of a nucleon with a nucleus. However, the data on these reactions are far from complete in providing a comprehensive picture of the field. This is certainly the case for the $pp \rightarrow pn\pi^+$ reaction. Recent detailed measurements near threshold have become available for this reaction [1–3] that seek to explore the role of *s*-wave pion production. Such low-energy pion results make important connections to soft pion theorems and chiral perturbation theory. Other investigations involving kinematically complete measurements [4,5] of differential cross sections and analyzing powers have been made at 800 MeV. In addition, analyzing powers and spin correlations have been investigated in a number of experiments in the energy range from 420 to 1250 MeV [6]. These investigations were strongly motivated by the structure observed in spin-dependent proton-proton scattering and their link to the possible existence of dibaryon resonances. In the energy range from 350 to 500 MeV few cross section and analyzing power data exist. A previous study reported inclusive measurements [7] of pion differential cross sections and analyzing powers at 400 and 450 MeV. These measurements covered a limited pion energy range and suffered from limited statistics. Earlier measurements in this energy range are discussed in Refs. [8–11]. A summary of the data sources in the literature on $NN \rightarrow NN\pi$ reactions up to about 1981 can be found in Ref. [12]. In the present study inclusive measurements are presented of pion differential cross sections and analyzing powers at 420 and 500 MeV that span the pion energy region from the onset of the three-body continuum down to pion energies as low as 25 MeV (lab). The angular range covered extended from 23° to 100° (lab). The internal np excitation energies range from 0 to about 80 MeV; thus relative np angular momentum values l_{np} greater than 0 will be important. Only $l_{np}=0$ (neglecting the deuteron *D* state) contributes to the $pp \rightarrow d\pi^+$ reaction. Contributions of these higher

---

*Present address: 120 Rothsay Avenue, Hamilton, ON, Canada L8M 3G1.

[†] Present address: #5-1665 Cotton Drive, Vancouver, B.C., Canada V5L 3V3.

[‡] Deceased.

[§] Present address: Department of Physics, The George Washington University, Washington, D.C. 20052.

l_{np} values in the $pp\rightarrow pn\pi^+$ reaction will be explored in this investigation.

A more detailed knowledge of the $pp\rightarrow pn\pi^+$ reaction is also important to further our understanding of the role of the primary $NN\rightarrow NN\pi$ reactions in the two-body $A(\vec{p},\pi^+)B$ reactions. This is discussed by Falk [13] in connection with a phenomenological model of the $A(\vec{p},\pi^+)B$ reaction.

II. THEORY

There are several theoretical models of the $NN\rightarrow NN\pi$ reaction appropriate to the energy range presently of interest. Ideally, both NN elastic scattering and single pion production should be predicted by the same theoretical model. One such unitary model is that of Dubach, Kloet, and Silbar [14]. A basic feature of this model is the careful attention given to two- and three-body unitarity. The predictions of this model for a variety of spin observables are in moderate agreement with experiment. Other groups have also developed unitary models, notably Matsuyama and Lee [15]. In this model provision is made for both the conventional meson exchange mechanisms and the possible dibaryonic excitations of six-quark states. More recently, Engel *et al.* [16] and Shyam and Mosel [17] have carried out calculations within a framework where the dynamics of the production process is described by a covariant effective one-boson-exchange model (CEOBEM). The final state interaction effects are treated in the Watson-Migdal theory [18]. In this model all the calculations are performed in a fully covariant manner. The model incorporates the exchange of π, ρ, σ, and ω mesons and treats both nucleon and delta isobar excitations as intermediate states. The propagation of the exchanged mesons and intermediate baryons is described by using the corresponding covariant propagators. The parameters of the model (coupling constants and cutoff masses) are determined by fitting to the NN scattering data over a range of beam energies [16]. Predictions from this model for the cross section distributions for the current experiment at 420 and 500 MeV will be presented. At the present time this model does not provide predictions of the analyzing powers.

A common classification of these reactions is provided by their isospin decomposition according to Rosenfeld [9], designated σ_{ij}. Here i is the isospin of the initial NN system and j is the isospin of the final NN system. The reactions that shall concern us in the present study are

$$\text{(a)}\ p+p\rightarrow d+\pi^+,\ \ \sigma^d_{10},$$

$$\text{(b)}\ p+p\rightarrow p+n+\pi^+,\ \ \sigma_{10}+\sigma_{11},$$

$$\text{(c)}\ p+p\rightarrow p+p+\pi^0,\ \ \sigma_{11}.$$

The two-body and three-body final states where the np system has $T=0$ are indicated by σ^d_{10} and σ_{10}, respectively. Much is known about σ^d_{10} from extensive cross section, analyzing power, and spin correlation measurements from investigation of the $pp\rightarrow d\pi^+$ reaction and its inverse [19]. On the other hand, σ_{10} is less well known, in part because any NN induced reaction that gives rise to σ_{10} is also accompanied by σ_{11} or σ_{01}. Thus the investigation of reaction (b) above, involves a combination of these two isospin terms.

TABLE I. Low-lying angular momentum states and partial wave amplitudes in the $pp\rightarrow pn\pi^+$ reaction.

		pp system			pn system				
	J^π	S	L	s_{pn}	l_{pn}	S'	L_π	Class	Amp
$T_{pn}=0$	1^-	1	1	1	0	1	0	Ss	a_1
	0^+	0	0	1	0	1	1	Sp	a_0
	2^+	0	2	1	0	1	1		a_2
	1^-	1	1	1	0	1	2	Sd	a_3
	2^-	1	1	1	0	1	2		a_4
	2^-	1	3	1	0	1	2		a_5
	3^-	1	3	1	0	1	2		a_6
	0^-	1	1	0	1	1	1	Pp	c_1
	1^-	1	1	0	1	1	1		c_2
	2^-	1	1	0	1	1	1		c_3
	2^-	1	3	0	1	1	1		c_4
	2^+	0	2	0	1	1	2	Pd	c_5
	1^-	1	1	1	2	1	0	Ds	c_6
	0^+	0	0	1	2	1	1	Dp	c_7
	2^+	0	2	1	2	1	1		c_8
	1^-	1	1	1	2	1	2	Dd	c_9
	2^-	1	1	1	2	1	2		c_{10}
	2^-	1	3	1	2	1	2		c_{11}
	3^-	1	3	1	2	1	2		c_{12}
$T_{pn}=1$	0^-	1	1	0	0	0	0	Ss	b_0
	2^-	1	1	0	0	0	2	Sd	
	2^-	1	3	0	0	0	2		
	0^+	0	0	1	1	0	0	Ps	b_1
	2^+	0	2	1	1	2	0		b_2
	1^-	1	1	1	1	0	1	Pp	
	0^-	1	1	1	1	1	1		
	1^-	1	1	1	1	1	1		
	2^-	1	1	1	1	1	1		
	2^-	1	3	1	1	1	1		
	2^+	0	2	1	1	0	2	Pd	
	2^+	0	2	1	1	1	2		
	2^+	0	2	0	2	2	1	Dp	

A further, more detailed, classification of the transitions occurring in the $pp\rightarrow pn\pi^+$ reaction is given in terms of the partial wave amplitudes. An analysis of the differential cross section and analyzing power distributions to extract these partial wave amplitudes will be presented in Sec. V C. Table I gives the low angular momentum states allowed in the

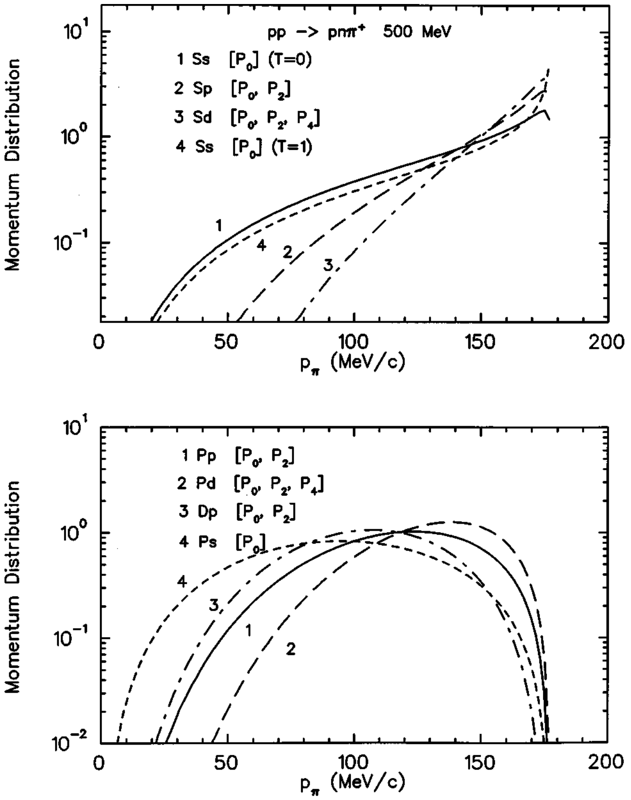

FIG. 1. Momentum distributions (c.m.) for the pion differential cross section as defined by Eq. (1) for the transition classes given in Table I. The possible Legendre polynomial terms that modulate each of these distributions are indicated.

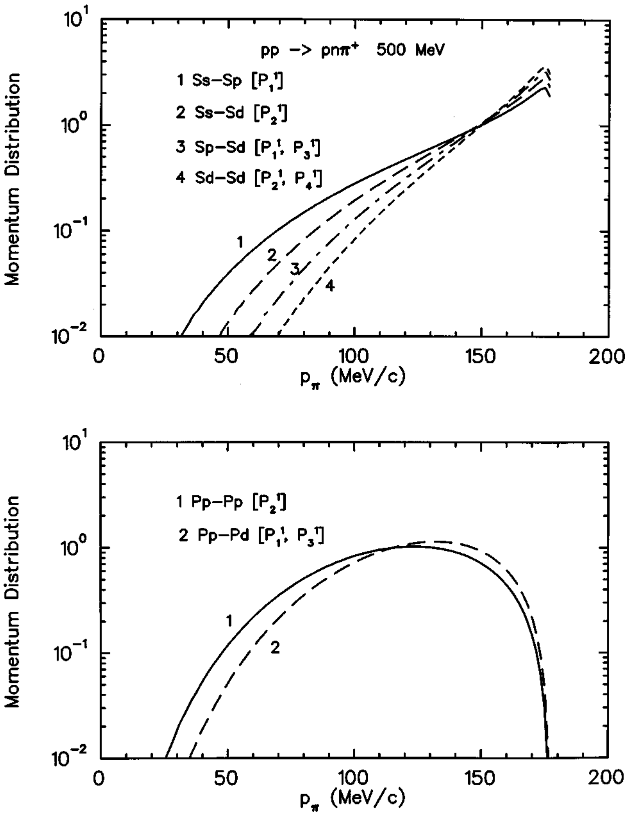

FIG. 2. Momentum distributions (c.m.) for the pion analyzing powers for the transition classes given in Table I. The possible associated Legendre polynomial terms that modulate each of these distributions are indicated.

$pp \rightarrow pn\pi^+$ reaction. Here T_{pn} is the isospin and s_{pn} and l_{pn} are the spin and orbital angular momentum of the final pn system, which combine to form the channel spin $\vec{S}' = \vec{s}_{pn} + \vec{l}_{pn}$. The pion orbital angular momentum is designated by L_π. The final column gives the partial wave amplitudes a_i in a notation which corresponds to that of Blankleider and Afnan [20] for the isoscalar $s_{pn}=1$ and $l_{pn}=0$ final states; for the isovector final states the b_i are the amplitudes defined by Daehnick [21]. The remaining isoscalar final states are designated with the amplitudes c_i. For the sake of brevity many of the partial wave amplitudes for channel spin $S' = 2,3$ and greater have not been shown.

The shape of the pion momentum distribution is determined by s_{pn}, l_{pn}, and L_π. In particular, the final nucleon states $^3S_1$ and $^1S_0$ give rise to a pronounced final state interaction (FSI) that greatly enhances the spectrum at low relative np energies. Following the designation used by Rosenfeld [9], the letters *S, P, D* are used to specify the orbital angular momentum state l_{pn}, and *s, p, d* to specify the orbital angular momentum state L_π. Together, these two letters specify the ''class'' of the transition, as shown by the second last column in Table I. A general discussion of the anticipated contribution to the cross section of these different classes, based on simple physical concepts (dependence of matrix element on momentum, phase space, final state interactions, etc.) has been presented by Rosenfeld [9]. Specifically, the phenomenological pion momentum distribution [9,10] can be expressed as

$$\frac{d\sigma}{dp_\pi} \propto \xi \frac{m_\pi}{E_\pi} \frac{\eta}{E_\pi} \eta^{2L_\pi+1} Q^{l_{pn}+1/2}. \tag{1}$$

Here $Q = T_0 - T_\pi$, where T_0 is the maximum pion kinetic energy and η is the pion momentum in units of $m_\pi c$. The expression comprises the square of the matrix element, proportional to $\eta^{2L_\pi} Q^{l_{pn}}$, and the phase space factor $\xi \eta Q^{1/2}$; $\xi = [m(Q+4m)]^{1/2}/(Q+2m)$, and m is the mean nucleon mass. The pion wave function includes the normalization factor $(m_\pi/E_\pi)^{1/2}$. Final state interactions are accounted for by multiplying the above expression by the term $1/(Q+E^*)$. For the $^3S_1$ pn nucleon state E^* is the binding energy of the deuteron (2.22 MeV), and for $^1S_0$ E^* is the energy of the antibound (or virtual) state (0.065 MeV).

Figure 1 illustrates the pion momentum distributions as defined by Eq. (1) for most of the transition classes given in Table I. These are center of mass (c.m.) distributions calculated for 500 MeV proton bombarding energy. For convenience and brevity, we will at times refer collectively to *Ss*, *Sp*, and *Sd* as *S*-class transitions, and to the others as *P*-class and *D*-class transitions, or even *P*/*D*-class transitions. All the *S*-class transitions are qualitatively similar, with their pronounced enhancement at high pion momentum (low np internal energy). However, the *Ss*-class distributions, because of the FSI, drop less rapidly with decreasing pion momentum. The remaining transition classes *Ps*, *Pp*, *Pd*, and *Dp* are also qualitatively similar. The c.m. momentum and angular dependence of the differential cross section is given by a linear combination of the momentum distributions multiplied by appropriate Legendre polynomial functions P_l; the multiplying functions that are permitted are noted in Fig. 1. The expression for the cross section (see Sec. V C) also contains interference terms between the different classes of transitions. For example, there are such interference terms from the Ss and Sd classes. In this particular case the corresponding shape of the momentum distribution is identical to that for the Sp transition class. More generally, interference between terms in the pion angular distribution can occur only if the final nucleon states are identical [9]. This immediately rules out the possibility of interference between terms from σ_{10} and σ_{11}.

Analyzing powers, which arise from such interference terms between different classes, as well as from interference within classes, also have associated momentum distributions which fall into two main groups. This is illustrated in Fig. 2. In parallel to that for the cross section, the expression for the c.m. momentum and angular dependence of the analyzing power is given by a linear combination of the momentum distributions multiplied by appropriate associated Legendre polynomial functions P_l^1; the multiplying functions that are permitted are noted in Fig. 2.

The expression for the pion angular dependence in the $pp\rightarrow pn\pi^+$ reaction in terms of the amplitudes defined in Table I is obtained from basic reaction theory [22] and is given by

$$\frac{d\sigma}{d\Omega}(\theta,\phi)_{[S\mu S'\mu']}=\Big|\sum_{LL_\pi J}(-1)^L\alpha^J_{L_\pi S'LS}(S\mu L0|J\mu)(S'\mu' L_\pi\mu-\mu'|J\mu)Y^{\mu-\mu'}_{L_\pi}(\theta,\phi)\Big|^2. \tag{2}$$

Here $\alpha^J_{L_\pi S'LS}$ represents the partial wave amplitudes, a_i, b_i, c_i. S and S' are the initial and final channel spins, respectively, L is the initial orbital angular momentum, and L_π the pion orbital angular momentum, as defined in Table I. The quantization axis is in the direction of the incident proton beam. Partial spin cross sections, more appropriate to the present case of a transversely polarized beam, are related in a simple way to the sums appearing in the above expression. The product terms of the spherical harmonics are easily reinterpreted in terms of the Legendre functions. Because of the very large number of terms that result, the coefficients of the products of the amplitudes $\alpha_i\alpha_j^*$ cannot be presented here. However, a comparison was made with the tabulation of Blankleider and Afnan [20] for those terms involving the a_i amplitudes. The present formulation led to expressions that were identical to those of Ref. [20] for the differential cross section and and the analyzing power.

III. THE EXPERIMENT

A. Polarized proton beam

The experiment was performed in the proton hall of the TRIUMF laboratory using the large acceptance second arm spectrometer (SASP). Polarized proton beams from the optically pumped polarized ion source (OPPIS) were extracted from the TRIUMF cyclotron at energies of 500 and 420 MeV, with a momentum dispersion on target of -11 cm/%. Beam intensities ranged from approximately 0.1 to 8 nA, depending on spectrometer angle and magnetic field setting, and the beam polarization was typically in the range from 70 to 75 %. The beam polarization P was measured using an in-beam polarimeter (IBP) (Ref. [23]).

Energy calibration of the incident proton beam was carried out using the measured pion energies for the $pp\rightarrow d\pi^+$ reaction, obtained from the acceptance calibration runs. From eleven measurements at each beam energy, the latter was determined to have the values $499.85\pm0.28\pm0.53$ MeV and $419.79\pm0.28\pm0.36$ MeV. The first error represents the standard deviation in the measurements, and the second the systematic error from the uncertainty in the reaction angle and the SASP momentum calibration.

The number of beam protons N_p was measured using the IBP and a secondary emission monitor (SEM) (Refs. [23,24]), positioned upstream and downstream of the target, respectively. These two instruments were calibrated in previous experiments using a Faraday cup and provided independent measurements of the beam intensity. A problem was uncovered with the SEM at very low beam intensities of ≈ 0.1 nA; in effect, the ratio of the SEM current to the IBP current increased at these currents by about 5%. An explanation consistent with these observations, and later qualitatively verified by measurement, was the existence of an SEM dark current. Empirical corrections were made to account for this. A second problem with the use of the SEM is that it is a charge integrating device with an output rate of <10 pulses/s at $I=1$ nA. Hence this device could not be used to measure separately the proton flux for spin up and spin down beam polarizations at the high spin-flip frequency of 40 Hz, since there are insufficient pulses from the integrator for each period of spin up or spin down. Consequently, the SEM was used to measure the total proton flux, and the IBP was used to determine the division of this total flux between the up and down spin states. Several further issues related to the beam flux measurements will be discussed in a later section.

B. Liquid hydrogen target

The target constructed for this experiment provided three target cells within the cryostat, one for liquid hydrogen (LH_2), one for liquid deuterium (LD_2), and an empty (dummy) cell for background measurements. In addition, a ZnS beam-viewing screen, backed with a layer of CH_2, was mounted outside of the cryostat. The actual LH_2 cell consisted of two 25.4 μm thick stainless steel foils mounted on a 0.5 cm thick ring, 7 cm in diameter. The absolute pressure within the cell of 16.0 to 16.5 psi resulted in bulging of the foils to produce a central cell thickness of 0.98±0.02 cm. Changes from one target cell to another could be accomplished remotely, while changes in target angle had to be made manually.

C. SASP spectrometer

Pions were detected in the SASP spectrometer [25]. This spectrometer is a quadrupole-quadrupole-dipole (QQD) magnetic system with a dispersion/magnification ratio of 4.7 cm/%. It has a solid angle exceeding 12 msr, depending on software cuts, and a momentum acceptance, expressed in terms of the percentage momentum deviation $\delta=[(p-p_0)/p_0]\times 100$, extending well beyond the -10 and $+15\,\%$ design limits. Here p_0 is the momentum of the central trajectory. Because of the relatively short flight path of about 7 m it is well suited for the detection of pions. The resolution at the design maximum central momentum of 660 MeV/c is $0.02\,\%\ \Delta p/p$. A detailed account of the design and operating parameters of the spectrometer has been presented [26]. It is instrumented with a front end multiwire drift chamber (FEC) at the entrance to the first quadrupole, and two vertical drift chambers (VDC1 and VDC2) and a scintillator hodoscope, comprising two layers of scintillators, at the exit of the dipole.

D. Data recording

The event trigger was defined in terms of coincident events in each of the scintillator elements and the first plane of VDC1. By not including the FEC in the event trigger considerably higher beam currents could be tolerated. Particle identification of the pions was obtained from particle time-of-flight (with respect to the cyclotron rf) and energy loss in the focal plane scintillator.

Each foreground run with the LH_2 target was accompanied by a background run with the empty (dummy) cell. In order to cover the full momentum range of the outgoing pions from the $pp\to pn\pi^+$ reaction up to five momentum settings of the spectrometer were required. The highest momentum setting for each angle was always chosen to position the peak from the $pp\to d\pi^+$ reaction at $\delta\approx 12\%$, where the acceptance of the spectrometer was still close to unity. The cross sections from this reaction were used for monitoring and normalization of the data.

IV. ANALYSIS

A. Data reduction

The event-recorded data were analyzed with the program NOVA [27]. Pion events were selected on the basis of their energy loss in the scintillator and time-of-flight (TOF) through the spectrometer. An example of this event selection is shown in Fig. 3, where well defined groups of pions and muons are identified. In some cases the TOF did not separate the two groups adequately and other means had to be used to effect the separation. This will be discussed in Sec. IV B. The large intensity of the muon group, relative to that of the pion group, will also be addressed there. The wire chamber information from the FEC and VDC's was used to reconstruct the particle trajectories. Aberration corrections in the bend-plane coordinate θ as defined in the TRANSPORT convention [28], had to be applied in order to optimize the resolution. Particle trajectories extrapolated back to the target position served as the basis for making cuts for the final event selection. Representative of the target distributions are the plots of Fig. 4, showing the position (X_i) and angle (θ_i) in the spectrometer bend plane, and the position (Y_i) and angle (ϕ_i) in the nonbend plane. Cuts were placed on these four variables at ±3.5 cm, ±100 mr, no cuts, and ±60 mr, respectively.

Each event was corrected for the mean energy loss in the target, corresponding to corrections of 0.5 to 2 MeV/c to the pion momentum. Because of the large acceptance of SASP (±43 mr in the scattering plane) a large kinematic spread is present. A correction was thus also applied that shifted the momentum value (preserving the same np invariant mass) to the value that would be observed at the central scattering angle of the spectrometer. Figure 5 shows a momentum spectrum taken at an angle of 24° and 420 MeV, for a field setting that includes the peak from the $pp\to d\pi^+$

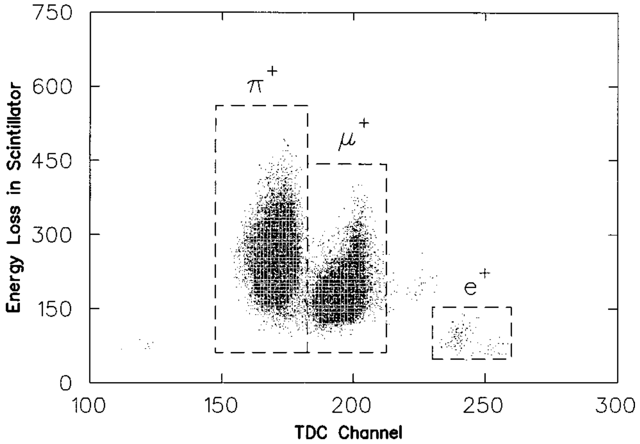

FIG. 3. Particle identification spectrum showing particle energy loss in the scintillator as a function of the output of the time to digital converter (TDC). The time scale is 0.25 ns/channel. Time of flight increases to the left.

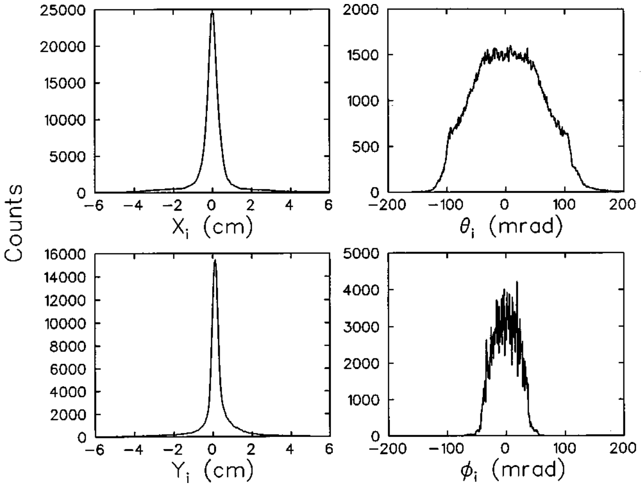

FIG. 4. Reconstructed pion trajectories at the target position showing the position (X_i) and angle (θ_i) in the spectrometer bend plane and the position (Y_i) and angle (ϕ_i) in the nonbend plane.

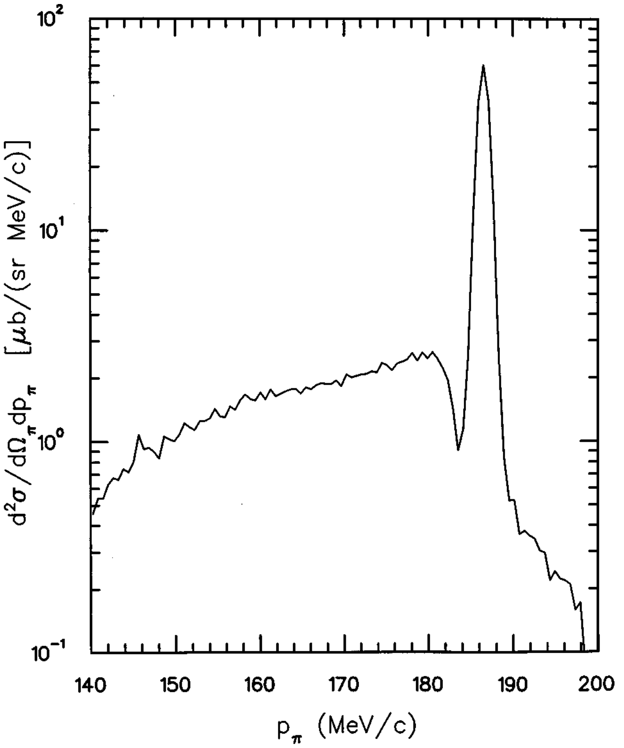

FIG. 5. Pion momentum spectrum taken at 420 MeV and 45°. The three-body continuum begins 2.5 MeV/c below the two-body peak.

reaction. The resolution is 1.1 MeV/c (FWHM), which is nearly adequate to effect a clean separation between the two-body peak and the onset of the continuum.

A composite wire chamber efficiency was determined as the ratio of the number of events where each of the chambers (FEC and VDC's) had one, and only one, properly decoded track, to the number of events identified as pions, together with a hit in one of the planes of the FEC. The VDC efficiency results were tested by further calculations where various combinations of 2, 3, and 4 VDC planes were considered. These showed the variations expected due to the correlations in the hit patterns for adjacent planes, but the veracity of the composite values as defined above was confirmed. The error $\epsilon_{\eta_{Ch}}$ in the calculated efficiency η_{Ch} is given by [29]

$$\epsilon_{\eta_{Ch}} = \sqrt{\frac{\eta_{Ch}(1-\eta_{Ch})}{N}},$$

where N is the number of times the efficiency condition is evaluated.

The computer livetime was defined as $\eta_{\text{live}} = \text{latch/event}$, where event is the number of events satisfying the trigger condition and latch is the number of events processed by the detector electronics. The error in this quantity is defined similarly to the error in η_{Ch}, above.

Corrections to the measured pion flux to account for the decay of pions in the spectrometer system were investigated in a Monte Carlo study. This study yielded an effective spectrometer length L_{eff}, from which the pion survival probability η_π was calculated using the expression

$$\eta_\pi = \exp[(-m_\pi c \times L_{\text{eff}})/(\tau c \times p_\pi)].$$

Here $\tau c = 7.804$ m, is the pion decay length. Because of the large acceptance of SASP this effective length depends on the central momentum setting of the magnet and on the focal plane position of the event. For central trajectories, L_{eff} varied from 7.6 m at 300 MeV/c to 8.3 m at 80 MeV/c.

The acceptance of the SASP spectrometer as a function of the percentage momentum deviation δ was calibrated using pions from the $pp \rightarrow d\pi^+$ reaction. Pion decay corrections, as well as all the other corrections made in the cross section calculations (discussed below), were applied.

In order to adequately account for the large variations in ϵ_{SASP} and η_π associated with different events, the quantity $1/(\epsilon_{\text{SASP}}\eta_\pi)$, was calculated and stored for each event. This event weight thus represents the yield information normalized for the relative spectrometer acceptance and the pion survival fraction.

The spin-dependent differential cross section for a given momentum interval was calculated according to the expression

$$d^2\sigma/d\Omega_\pi dp_\pi = N_\pi / [\eta_{Ch}\eta_{\text{live}} N_p N_t \Delta\Omega_\pi \Delta p_\pi].$$

Here N_π is the number of events, normalized for the relative spectrometer acceptance and the pion survival fraction, as discussed above, and N_p and N_t are the number of incident protons and the number of target nuclei per cm^2, respectively. The solid angle is given by $\Delta\Omega_\pi$ and the pion momentum interval is Δp_π. This expression applies to the total, spin up or spin down cross section, according to the selected input quantities. The background subtracted cross section was next calculated

$$d^2\sigma/d\Omega_\pi dp_\pi = d^2\sigma/d\Omega_\pi dp_\pi(\text{LH}_2) - d^2\sigma/d\Omega_\pi dp_\pi(\text{dummy}).$$

Denoting the differential cross section of the above expression simply by σ, for brevity, the spin averaged differential cross section is given by

$$\sigma = \frac{[P(\downarrow)\sigma(\uparrow) + P(\uparrow)\sigma(\downarrow)]}{[P(\uparrow) + P(\downarrow)]}.$$

Here ↑ and ↓ refer to the spin up and spin down direction of the incident beam polarization, respectively. The analyzing power is given by the expression

$$A_{N0} = \frac{[\sigma(\uparrow) - \sigma(\downarrow)]}{[P(\downarrow)\sigma(\uparrow) + P(\uparrow)\sigma(\downarrow)]}.$$

B. Pion decay and muon background

Pion decay corrections discussed previously account for the loss of pion flux because of the ≈8 m distance between the target and the scintillator hodoscope. Two other problems related to pion decay were identified in this experiment. The first is related to the measurement of a low cross section continuum in the presence of a large flux of pions in the target region. For example, at 500 MeV and a spectrometer angle of 24°, pions from the $pp \rightarrow d\pi^+$ reaction and the early part of the continuum from the $pp \rightarrow pn\pi^+$ reaction,

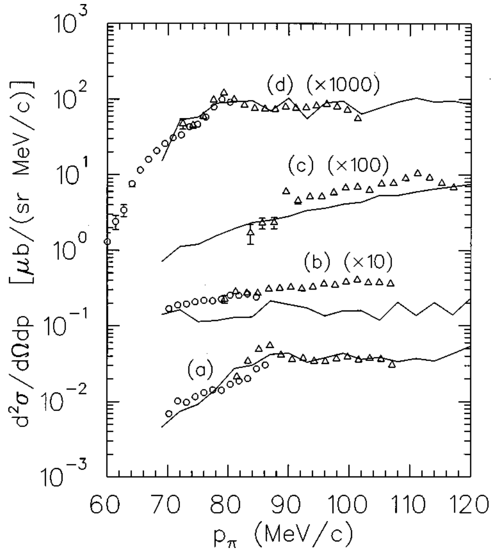

FIG. 6. Measured muon spectra, together with the Monte Carlo predictions (solid line), (a) 420 MeV, 55°, (b) 420 MeV, 75°, (c) 500 MeV, 24°, (d) 500 MeV, 85°.

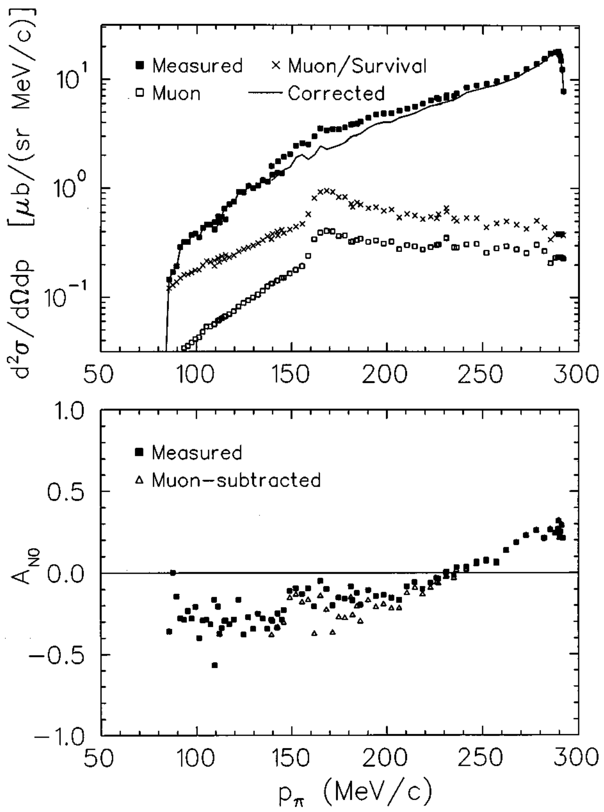

FIG. 7. Momentum distributions before and after subtraction of the muon background for 500 MeV and 24°.

have momenta of ≈290 MeV/c and give rise to decay muons with momenta of 160 to 300 MeV/c. These muons are strongly focussed in the direction of the original pion velocity. While the flux of muons at the higher momentum is not significant relative to the strength of the detected pion flux, this is not the case for the 160 MeV/c muons, where the pion continuum cross section is already much lower. Furthermore, the muons, with their 2.2 μs lifetime suffer negligible decay, unlike the pions.

A second Monte Carlo study was undertaken to investigate the transport of muons, generated between the target and the entrance of the spectrometer, to the top end detection system. The pion flux generated at the target was modeled from the currently measured $pp \to d\pi^+$ and $pp \to pn\pi^+$ cross sections. Fortunately, in some of the continuum measurements good TOF separation between pions and muons was achieved, and these could be used to test the Monte Carlo predictions. In Fig. 6 several such comparisons between the measured and predicted muon spectra are presented. The agreement is not uniformly good, which is not too surprising since the muon-generating pion flux, and its transport through the system, could be modeled only approximately. However, while the intensity of the muon spectrum was subject to considerable uncertainty, the calculated shape was judged to be much more reliable. In addition, the degree of separation of the muons from the pions had to be estimated in the pion identification spectrum, before the subtraction could be made. Consequently, the calculated muon spectrum was normalized to the experimental muon spectrum and a 30% error included in the subtraction. Figure 7 shows the complete momentum distribution of the differential cross section and analyzing power for 500 MeV and 24° before and after correction for the muon background. Since the muons have a 2.2 μs half life the calculated muon spectrum was divided by the pion survival fraction before carrying out the subtraction. The bump which appears at ≈160 MeV/c arises from the decay of pions from the $pp \to d\pi^+$ reaction, where the muon is produced at 180° in the pion center of mass frame. The positive analyzing power of the $pp \to d\pi^+$ reaction is reflected in the bump in A_{N0} at this same momentum. The corrected analyzing power is given by

$$A_c = \frac{\sigma_m A_m - \sigma_\mu A_\mu}{\sigma_m - \sigma_\mu},$$

where σ_m is the measured unpolarized cross section, σ_μ the muon unpolarized cross section, and A_c, A_m, and A_μ are the corrected, measured, and muon background analyzing powers, respectively. For this particular angle the correction seems to be underestimated, since the corrected spectrum for the analyzing power still exhibits a slight bump at ≈160 MeV/c.

A second effect of pion decay is the presence of long tails at the base of the approximately Gaussian momentum response function of the system. The main Gaussian component had a typical width [full width at half maximum (FWHM)] of about 2 MeV/c for 300 MeV/c pions, most of which is contributed by the energy loss spread in the target. Tails on this peak arise from decay muons that have momenta and directions very close to those of the originating pions and are sufficiently similar in their TOF that they cannot be distinguished from pions. Assuming symmetry, the tail on the low-momentum side of the $pp \to d\pi^+$ reaction peak was approximated by the measured tail on the high-momentum side of the peak, and directly subtracted. The strength of this tail and the effect of subtraction from the continuum is shown in Fig. 8; typically these tails represented a 2 to 15 % background in the region where the continuum was at its maximum. Finally, a response function for

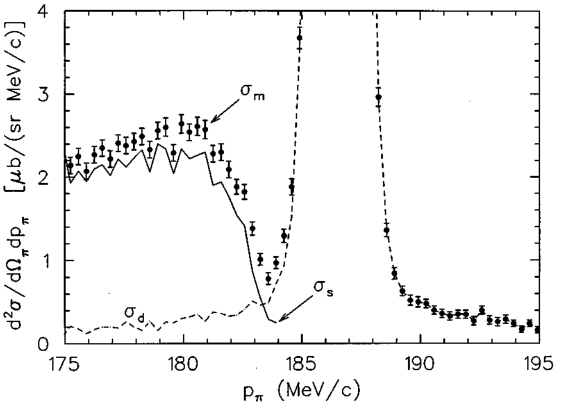

FIG. 8. Subtraction of the tail on the $pp\rightarrow d\pi^+$ reaction peak from the $pp\rightarrow pn\pi^+$ reaction continuum. The tail from the $pp\rightarrow d\pi^+$ peak is represented by σ_d which, after subtraction, yields σ_s.

the magnetic spectrometer to a monoenergetic pion group was defined from the measured tails and used to perform a deconvolution of the continuum. This deconvolution resulted in the subtraction of a nearly linear background varying from 6 to 13% of the measured spectrum over the range from 80 to 300 MeV/c.

C. Results

The experimental distributions of the differential cross sections and analyzing powers, after corrections for the above effects, are shown in Figs. 9–12. The curves shown in these figures will be discussed in Secs. V and VI. An evaluation of the normalization uncertainties and the errors in the data is presented in the following section. Here we make several observations about the data, insights for which became apparent during detailed fitting and the extraction of the partial wave amplitudes. At 420 MeV and 25.1°, as shown in Fig. 9, data from the highest momentum spectrometer bite does not match smoothly with the data from the second bite in the region of ≈175 MeV/c. The problem seemed to be with the highest momentum bite data in the region ≈173–190 MeV/c. Fortunately, the number of such data points is relatively small compared with the much larger number near the peak. The outcome of the analysis was not strongly influenced by these points. At the same energy and at 34.9° the cross section over most of the pion momentum range was considerably larger than that of any plausible fit subsequently made; these data were considered to be unreliable and were omitted from the fitting procedure. Whether the problem with these data is a result of muon contamination, which was not properly accounted for in the background subtraction procedure, or some other effect, remains unclear.

D. Normalization and errors

1. Statistical errors

Statistical uncertainties were calculated for all the quantities that enter the expressions for the cross sections and analyzing powers $[N_\pi, \eta_{Ch}, \eta_{\text{live}}, N_p, P(\uparrow)$, and $P(\downarrow)]$. Typically these errors were very small in all, except possibly the first quantity. In addition, statistical errors arising from the muon subtraction, the subtraction of the tails on the peak, and finally the deconvolution, were added in quadrature to the above. In Figs. 9–12 these combined statistical errors are shown.

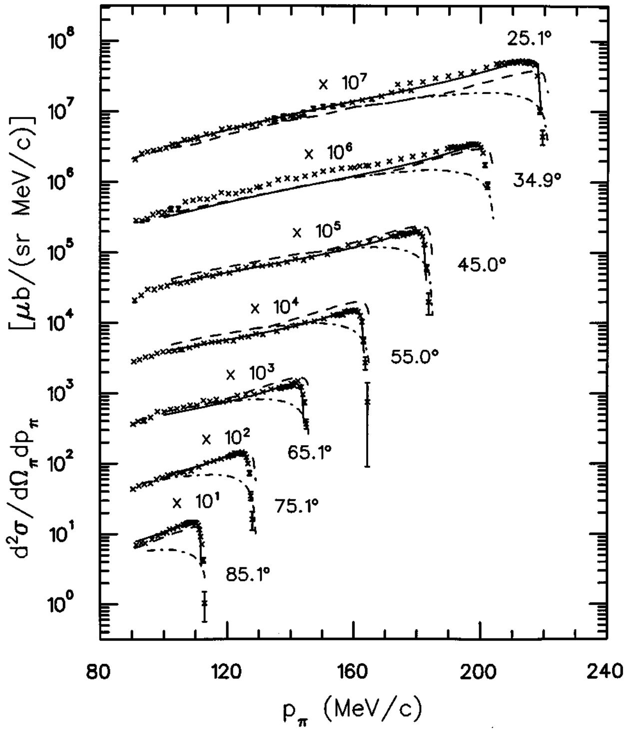

FIG. 9. Differential cross section distributions for the $pp\rightarrow pn\pi^+$ reaction at 420 MeV. The errors shown on the data points are the statistical errors only. The solid line is a fit to the data according to Eq. (6). The dashed line is a calculation from the covariant one-boson-exchange model that includes FSI effects. The dot-dash line is a calculation without FSI effects.

2. Systematic errors

The solid angle of the SASP spectrometer depends in a complex way upon the cuts applied to the reconstructed particle trajectories. Generous cuts were used in the current experiment and this, together with the experience of earlier studies, led to an estimation of the solid angle of $\Delta\Omega = 13.5 \pm 4\%$ msr. Target thickness uncertainty, noted in Sec. II B, contributed a ±2% error, and the target angle uncertainty, ±1%. Normalization of the pion yield to account for the SASP acceptance and the pion survival fraction, as expressed through ϵ_{SASP} and η_π (Sec. III A), contributed a ±3% error. From the experimental calibration data of the SEM and IBP the estimated error in the proton flux measurement is ±2% for each device. For the IBP this does not include the uncertainty in the thickness of the CH_2 polarimeter target; the latter is difficult to establish, given the large variations in density that characterize commercially available CH_2 foils. For this reason the SEM was used for the absolute proton flux measurement. Combining the above errors yields a normalization uncertainty from these sources in the cross section data of ±6%.

However, through the use of two different CH_2 foils in the IBP at each of the two beam energies it was established

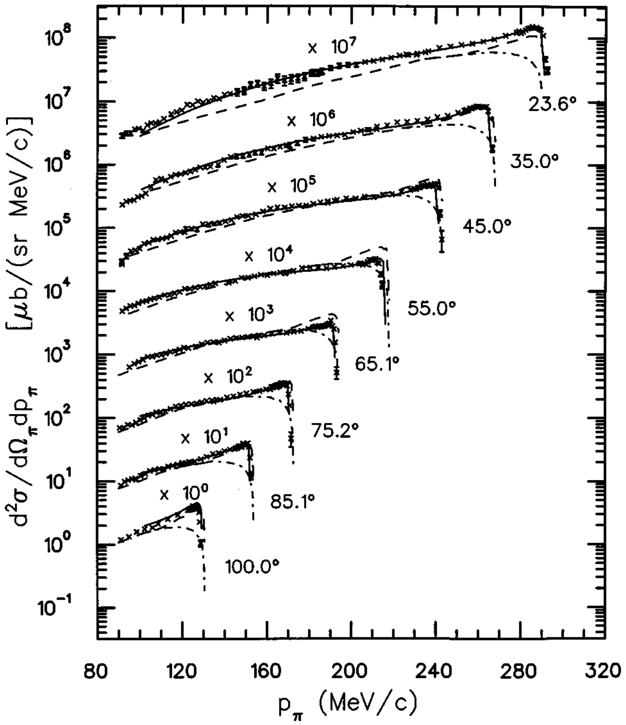

FIG. 10. Differential cross section distributions for the $pp \rightarrow pn\pi^+$ reaction at 500 MeV. The errors shown on the data points are the statistical errors only. The solid line is a fit to the data according to Eq. (6). The dashed line is a calculation from the covariant one-boson-exchange model that includes FSI effects. The dot-dash line is a calculation without FSI effects. The 55° and 100° data were taken without the FEC and are subject to an additional 10% normalization uncertainty.

that there was an internal inconsistency of about 6% in the proton flux measurements at the two energies. If it is assumed that the IBP gives the correct relative proton flux (since it depends on the well known pp elastic cross section), then the total charge measured by the SEM is ≈6% low at 420 MeV, relative to that at 500 MeV. Calculated cross sections at 420 MeV will be correspondingly high by this amount. In anticipation of the $pp \rightarrow d\pi^+$ reaction results, discussed below, all the 420 MeV cross section data were reduced by 6%.

3. $pp \rightarrow d\pi^+$ reaction results

A measurement of the differential cross section and analyzing power of the $pp \rightarrow d\pi^+$ reaction was automatically included at each of the angles for which measurements of the $pp \rightarrow pn\pi^+$ reaction were carried out. These measurements provided important checks on the data extraction procedures and ultimately on the cross section normalization and beam polarization. The results are shown in Table II, together with the accepted values obtained from SAID [30]. Only the statistical errors are indicated for the measured data. As explained above, the 420 MeV cross section data have been reduced by 6%. The agreement of the measured and accepted values of the analyzing powers is very good at both energies, with differences typically about 0.01. The cross sections at 500 MeV tend to be lower than the SAID values by 0.9±1.9%, while at 420 MeV the cross sections are higher than the SAID values by 1.6±2.8%. The overall agreement of the measured $pp \rightarrow d\pi^+$ cross sections with those of SAID are thus well within the bounds of the normalization uncertainty of ±6%.

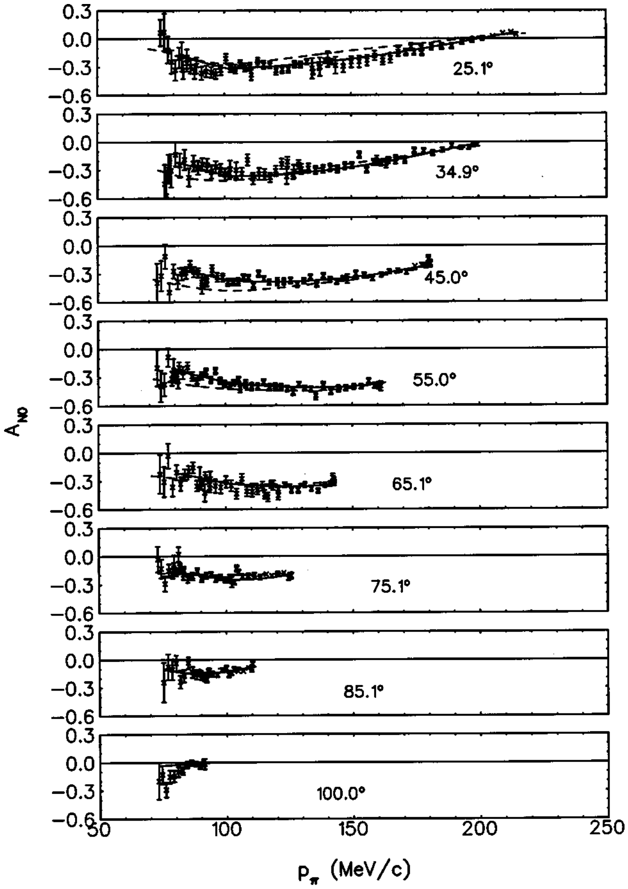

FIG. 11. Analyzing power distributions for the $pp \rightarrow pn\pi^+$ reaction at 420 MeV. Errors shown on the data points are the statistical errors only. The solid line is a fit to the data according to Eq. (7). The dashed line is an application of the FSI prediction according to Eq. (8).

Also shown in this table, under the heading PPID, are values for the $pp \rightarrow d\pi^+$ reaction calculated from a parametrization of the Bugg amplitudes [19] as discussed in Falk [13]. These also are in good agreement with both SAID and the current experimental measurements, and are used in the final state interaction model calculations described in the following section.

4. $pp \rightarrow pn\pi^+$ reaction results

In addition to the normalization uncertainty of 6% applicable to the $pp \rightarrow d\pi^+$ reaction, several further normalization uncertainties apply to the $pp \rightarrow pn\pi^+$ reaction. These arise from the uncertainty in the muon background (±6%) and the uncertainty in the subtraction of the tails on the peak and the deconvolution (±5%). Adding these quantities results in a normalization uncertainty of ±10% for the $pp \rightarrow pn\pi^+$ reaction data.

A comparison of the present data with the data from Ref. [7] was made by plotting the peak cross sections as a function of the pion lab angles. Since the energies for the present measurements are 420 and 500 MeV, vs 400 and 450 MeV for the earlier ones, only a general observation can be made:

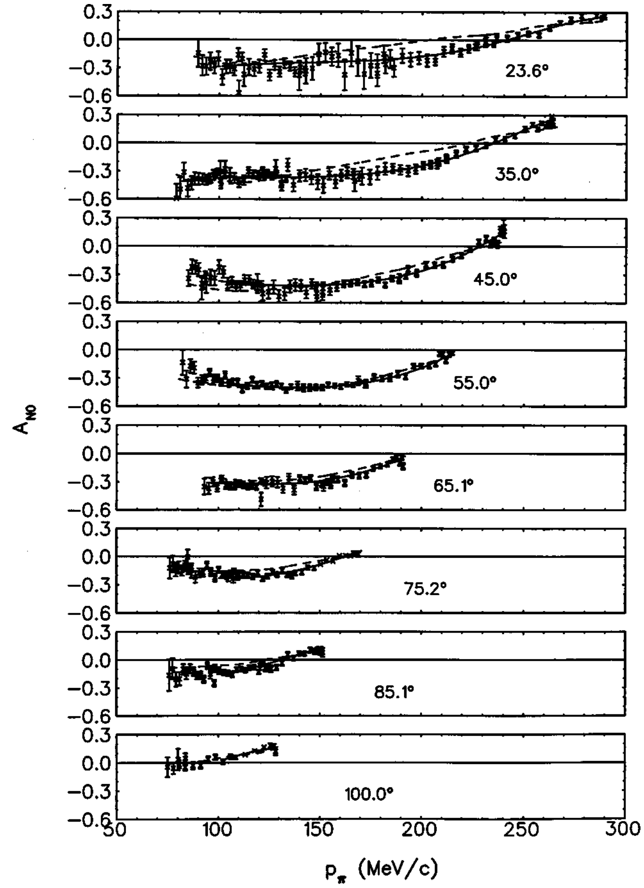

FIG. 12. Analyzing power distributions for the $pp\rightarrow pn\pi^+$ reaction at 500 MeV. Errors shown on the data points are the statistical errors only. The solid line is a fit to the data according to Eq. (7). The dashed line is an application of the FSI prediction according to Eq. (8).

the two data sets appear entirely consistent in terms of the magnitudes and the angular dependence of the peak cross sections.

V. COMPARISON WITH MODEL CALCULATIONS

A. Final state interaction model

While the agreement of the present experiment for the $pp\rightarrow d\pi^+$ reaction cross sections with expected values is very satisfactory, as discussed above, this is not necessarily sufficient confirmation for the veracity of the $pp\rightarrow pn\pi^+$ reaction cross sections. This is so because of the continuum nature of the latter reaction and the smallness of the cross section. An independent assessment of the cross section near the onset of the continuum can be made through a comparison with the two-body $pp\rightarrow d\pi^+$ reaction as described below.

For reactions such as $pp\rightarrow(pn)\pi^+$, where there is a final (pn) pair that can remain in a bound, as well as an unbound state, Boudard *et al.* [31] have shown that a simple relationship connects the amplitudes for the two processes. The expression of this relationship is

$$M(pp\rightarrow\{np\}_k\pi^+) = -\sqrt{\frac{2\pi m}{\alpha_t(k^2+\alpha_t^2)}}e^{-i\delta}M(pp\rightarrow d\pi^+). \tag{3}$$

Here $\alpha_t=\sqrt{m\epsilon}$, where m is the average nucleon mass, ϵ is the deuteron binding energy, and δ is the uncoupled S-wave triplet phase shift at relative momentum $\vec{k}$. The basis for this relationship is the observation that when a scattering wave function is extrapolated to the bound state pole, the result is proportional to the bound state wave function. Hence for S-wave proton-neutron scattering

$$\lim_{k\rightarrow i\alpha_t}\left\{-\sqrt{\frac{\alpha_t(k^2+\alpha_t^2)}{2\pi}}e^{-i\delta}\psi_k^{t(-)}(r)\right\} = \psi_d(r). \tag{4}$$

By introducing the phase space factors for the two- and three-body final states into the expressions for the respective cross sections, and making several kinematic approximations, they obtain

$$\frac{d^2\sigma}{d\Omega dx}(pp\rightarrow\{np\}\pi^+) = \frac{p(x)}{p(-1)}\frac{\sqrt{x}}{2\pi(x+1)} \times\frac{d\sigma}{d\Omega}(pp\rightarrow d\pi^+). \tag{5}$$

The internal excitation energy of the np system Q is related to x through the expression $x=Q/\epsilon=k^2/m\epsilon$. In the overall c.m. frame, $p(x)$ is the momentum of the pion in the $pp\rightarrow pn\pi^+$ reaction and $p(-1)$ the momentum of the pion in the $pp\rightarrow d\pi^+$ reaction. These quantities are evaluated at the same c.m. energy, hence the same bombarding energy.

Implicit in the above analysis is that the quantum numbers of the np pair are the same as those of the deuteron, namely, $S=1$ and $T=0$. These restrictions thus limit the applicability of the model to the σ_{10} cross section, and only pn S waves. Boudard *et al.* [31] have applied the above model to the cross section data of the $pp\rightarrow pn\pi^+$ reaction at 400 and 450 MeV (Ref. [7]). Within the limited range $Q<20$ MeV of the data, and the rather large statistical errors, very good agreement was observed.

We have used this model and carried out a simultaneous fit to the present data at all angles over a small range of excitation energy. Since the σ_{11} cross section is already significant, even at 420 MeV, this contribution was first subtracted from the experimental data. The details on the σ_{11} cross section are given in Sec. V B. The independent cross section data for the $pp\rightarrow d\pi^+$ reaction that was used in this comparison was obtained from the parametrization PPID, as noted in connection with Table II. Results of this fitting procedure are shown in Figs. 13 and 14, at 420 MeV and 500 MeV, respectively. The χ^2 values (per degree of freedom) for the fits were 3.0 and 4.2, with absolute normalizations (defined as $\sigma_{\mathrm{exp}}/\sigma_{\mathrm{th}}$) of 0.98 and 0.96, at 420 MeV and 500 MeV, respectively. Primarily, the large χ^2 values appear to arise from differences in the angular distributions between the experimental data and the input $pp\rightarrow d\pi^+$ reaction values. It should be noted that the steeply rising portion of the curves were not included in the fit. Also, for the 55° spectrum at 500 MeV, where the FEC chamber data were missing, a shift in the momentum scale of a few MeV/c is apparent between the experimental data and the calculated

TABLE II. Experimental values of the $pp \rightarrow d\pi^+$ differential cross sections and analyzing powers, together with the predictions PPID and SAID. The cross sections are given in the lab frame. Statistical errors only are shown; the overall normalization uncertainty is $\pm 6\%$.

T_p	$\theta_{\rm lab}$	$d\sigma/d\Omega$ (μb/sr)			A_{N0}		
(MeV)	(deg)	Exp	PPID [a]	SAID [b]	Exp	PPID [a]	SAID [b]
500	23.6	670.5±3.3	695.0	698.3	0.286±0.006	0.239	0.262
	35.0	370.9±1.5	377.1	377.1	0.239±0.005	0.202	0.230
	45.0	201.4±1.4	204.3	202.8	0.121±0.009	0.084	0.103
	55.0		130.6	128.8	−0.013±0.007	−0.027	−0.027
	65.1	114.4±0.5	116.3	115.0	0.016±0.005	−0.002	−0.004
	75.2	122.8±0.5	124.3	123.8	0.101±0.004	0.083	0.089
	85.1	136.3±0.7	133.0	132.9	0.164±0.007	0.141	0.154
	100.0		133.6	134.0	0.212±0.006	0.173	0.186
420	25.1	298.9±0.9	292.3	297.0	0.073±0.003	0.058	0.079
	34.9	182.1±0.8	169.0	171.9	−0.013±0.004	−0.031	−0.007
	45.0	93.6±0.5	93.9	92.4	−0.184±0.007	−0.209	−0.199
	55.0	61.4±0.5	63.2	60.2	−0.349±0.008	−0.344	−0.367
	65.1	58.1±0.3	56.9	55.3	−0.317±0.006	−0.294	−0.307
	75.1	58.9±0.2	59.5	59.7	−0.164±0.005	−0.167	−0.162
	85.1	63.2±0.2	62.1	63.3	−0.071±0.004	−0.071	−0.059
	100.0		60.4	61.4	0.006±0.006	0.002	0.014

[a] From the parametrization discussed in Ref. [13].

[b] From phase shift solution SP94 of Ref. [30].

curve. Nevertheless, given that the calculation represents an absolute independent assessment of the cross section, the agreement is very good.

B. Contribution of σ_{11}

An estimate of the pion production cross sections defined in the introduction can be obtained from the isospin decomposition parametrization of VerWest and Arndt [32]. For σ_{10}^d, σ_{10}, and σ_{11} the values (in μb) are 1047, 704, and 120, respectively, at 420 MeV, and 2224, 1945, and 494, respectively, at 500 MeV. Thus, while the σ_{11} cross sections are considerably smaller than the σ_{10} cross sections, they are not negligible. Moreover, the c.m. angular distribution of the differential cross section corresponding to the σ_{11} term is quite different from that for the σ_{10} term, and this may have a large effect on the shape of the pion momentum distributions in the laboratory frame.

Experimental data on the σ_{11} cross section is available through a number of studies, and particularly the study of the $pp \rightarrow pp\pi^0$ reaction [33]. In the common form in which this differential cross section is generally expressed $d\sigma/d\Omega \propto \frac{1}{3} + b\cos^2\theta$, $b \approx 0.05$ with a large uncertainty, and approximately constant from 400 to 700 MeV. The energy dependence of σ_{11} deduced in the $pp \rightarrow pp\pi^0$ reaction study can not be used directly in the $pp \rightarrow pn\pi^+$ reaction, because of the difference in the masses of π^+ and π^0. It is reasonable to assume that the cross sections will be approximately equal at the same c.m. pion momenta. In this manner the σ_{11} cross sections at 420 and 500 MeV in the $pp \rightarrow pn\pi^+$ reaction were estimated to have values of 69 and 502 μb, respectively. The latter value is in good agreement with the VerWest and Arndt value quoted above, while the one for 420 MeV is much lower. Values for b of 0.054 and 0.041 were used at 420 and 500 MeV, respectively.

The shapes of the c.m. pion momentum distributions were modelled from the ones given in the $pp \rightarrow pp\pi^0$ study, as expressed by Eq. (1). These are nearly symmetrical bell-shaped functions, dropping to zero at the minimum and maximum pion momentum. Final state interaction effects at the maximum pion momentum appear to be quite small above 400 MeV.

From the complete specification of the c.m. differential cross section for the σ_{11} term, laboratory pion momentum distributions were generated for each of the angles of the $pp \rightarrow pn\pi^+$ reaction study. These results did, indeed, indicate that the σ_{11} term makes a large relative contribution to the spectrum, particularly for c.m. angles around 90°.

C. Partial wave amplitude analysis

The formalism introduced in Sec. II leads to the following expression for the c.m. pion differential cross section:

$$4\pi \frac{d^2\sigma}{d\Omega_\pi dp_\pi}(\theta_\pi, p_\pi) = \sum_{\gamma,l} A_{\gamma l} f_\gamma(p_\pi) P_l(\cos\theta_\pi). \quad (6)$$

The symbol γ on the pion momentum distribution function $f_\gamma(p_\pi)$ labels the transition class (or classes) that are represented in the distribution (see Fig. 1). Each of these momentum distribution functions was normalized to unity, namely, $\int f_\gamma(p_\pi) dp_\pi = 1$. The $A_{\gamma l}$ comprise bilinear sums of the products of the partial wave amplitudes $\mathrm{Re}(\alpha_i \alpha_j^*)$ defined in Table I. In addition, they include all the angular momentum coupling terms that arise from Eq. (2). These quantities are treated as the unknowns in the fitting procedure and their

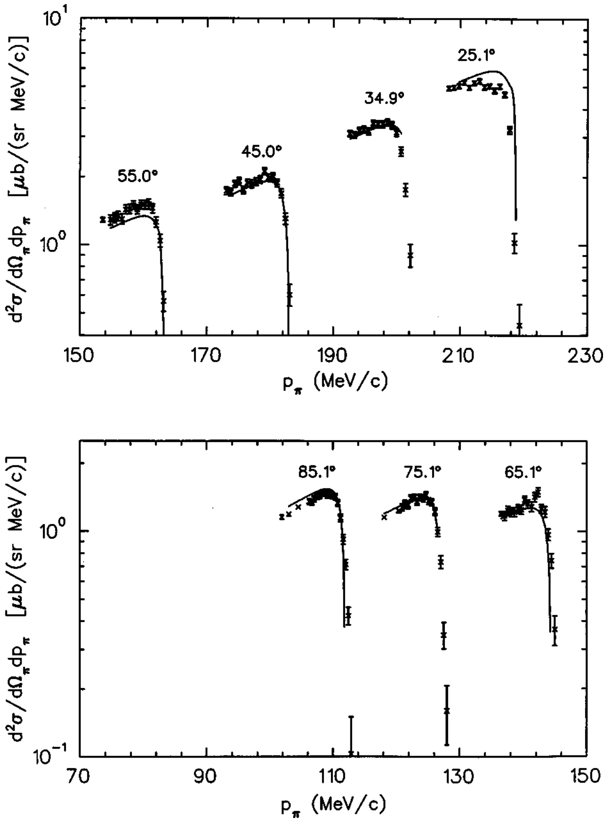

FIG. 13. Final state interaction fits according to Eq. (5) to the peak region of the momentum distributions at 420 MeV.

values extracted from the data. Knowledge of the $A_{\gamma l}$ thus provides a measure of the strength of a particular class of transitions. However, the strength of the individual amplitudes (or product of amplitudes) within a given class of transitions, cannot be determined from this procedure, since there is insufficient information available. In a similar fashion the expression for the analyzing power distribution is given by

$$4\pi \frac{d^2\sigma}{d\Omega_\pi dp_\pi}(\theta_\pi,p_\pi)A_{N0}(\theta_\pi,p_\pi) = \sum_{\gamma,l} B_{\gamma l} g_\gamma(p_\pi) P_l^1(\cos\theta_\pi), \tag{7}$$

where the $B_{\gamma l}$ comprise bilinear sums of the products of the partial wave amplitudes $\mathrm{Im}(\alpha_i \alpha_j^*)$, and $g_\gamma(p_\pi)$ is the momentum distribution function (see Fig. 2).

Since an experimental pion momentum distribution at a fixed laboratory angle represents a wide range of c.m. angles, it was most convenient to transform the theoretical distributions, represented by Eqs. (6) and (7), to the laboratory frame, rather than to transform the experimental data to the c.m. frame. The laboratory theoretical functions were then used in a fit to the experimental data for all the angles simultaneously to extract, first the $A_{\gamma l}$, and subsequently the $B_{\gamma l}$. Typically these fits involved about 200 data points at 420 MeV and about 350 data points at 500 MeV.

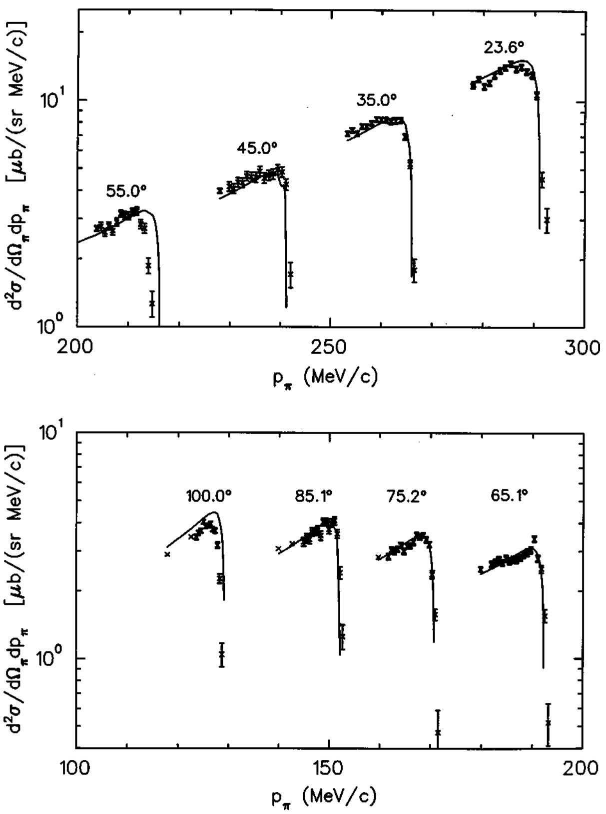

FIG. 14. As above, for 500 MeV. The 55° and 100° data were taken without the FEC and are subject to an additional 10% normalization uncertainty.

1. Cross sections

Such fits to the cross section distributions are shown by the solid lines in Figs. 9 and 10 for 420 and 500 MeV, respectively. With the exception of the high momentum part of the 25.1° spectrum and the 34.9° spectrum at 420 MeV (as explained in Sec. IV C) these curves represent generally good fits to the data over the whole momentum ranges for all the angles. Nevertheless, the χ^2 values (per degree of freedom) for these fits was unusually high at ≈ 5. A likely explanation for this lies in the difficulty of representing the SASP acceptance and pion decay correction over the very wide acceptance of the spectrometer. Despite the calibrations and modeling of these effects the data at the ends of a given momentum bite did not always match smoothly with the adjacent bites. The contribution to the χ^2 because of such mismatching is large. By adding a 3% error to each data point these χ^2 were reduced to values less than 2.

What is well established from the fitting procedure are the overall coefficients $A_l = \Sigma_\gamma A_{\gamma l}$, i.e., the coefficients of the Legendre polynomials. The results are given in Table III, and represent an average over a number of fits where different input assumptions and constraints were used. Of the two sets of results shown for 420 MeV, the first one does not include a P_4 term in the fitting procedure. The second fit shows that including a P_4 term alters the P_2 term about 10%. Only the fitting errors are shown in the table; not included is the overall data normalization uncertainty. The total cross section is given by the coefficient of P_0. Since the σ_{11} cross section was first subtracted before the fitting procedure was carried out, the coefficients of 681 and 2266 μb represent the σ_{10}

TABLE III. Coefficients $A_l=\Sigma_\gamma A_{\gamma l}$ (μb) in the Legendre polynomial expansion P_l of the differential cross section for the $pp\rightarrow pn\pi^+$ reaction.

	P_0	P_2	P_4	
420 MeV	665 ± 7	539 ± 8		[a]
	681 ± 11	604 ± 42	71 ± 10	
	1047	1147	43	$pp\rightarrow d\pi^+$
500 MeV	2266 ± 9	2103 ± 42	68 ± 53	
	2300	2437	-107	$pp\rightarrow d\pi^+$

[a] P_4 term not included in this fit.

total cross sections. As noted in Sec. V B the formulation of VerWest and Arndt [32] gives values of 704 and 1945 μb, respectively. The P_4 coefficients are poorly established; at both energies the improvement in the χ^2 obtained by including a P_4 term was negligible.

Also shown in Table III are comparison results for the $pp\rightarrow d\pi^+$ reaction. These were obtained from the parametrization PPID, discussed in Sec. IV D 3, evaluated at the same bombarding energy of 420 and 500 MeV. The P_0 and P_2 coefficients are observed to be comparable for both reactions and for both energies. This reflects the dominance of the a_2 resonant amplitude. The presence of this amplitude alone leads to equal P_0 and P_2 coefficients.

2. Analyzing powers

Fits to the analyzing power distributions are shown by the solid lines in Figs. 11 and 12 for 420 and 500 MeV, respectively. Unlike the situation for the cross section distributions, here no subtraction for the σ_{11} analyzing powers was first made to the data; these analyzing powers are only poorly established [33]. Consequently the fits represent results for the measured experimental analyzing powers, comprising σ_{10} and σ_{11}. Equation (7) requires cross section input data; the fitted results from the above section (including σ_{11}) were used for this. These fits, using only the statistical uncertainties in the data points, resulted in χ^2 values close to unity. The extracted coefficients of the associated Legendre polynomials are given in Table IV. Once again, the table entries represent an average over a number of fits where different input assumptions and constraints were used. Of the two sets of results shown for 420 MeV, the first used only *S*-class terms in the fit. The difference between it and the second entry suggests that P/D-class terms are not important at 420 MeV.

Table IV also shows the associated Legendre polynomial coefficients for the $pp\rightarrow d\pi^+$ reaction. These were once again obtained from the paramterization PPID, and evaluated at the bombarding energies of 420 and 500 MeV. A simple comparison between the reactions cannot be made in this case because the analyzing power is very sensitive to any additional terms that are present in the $pp\rightarrow pn\pi^+$ reaction (including, of course, the contribution of σ_{11}). Thus, for example, the P_1^1 term at 500 MeV has opposite signs for the $pp\rightarrow pn\pi^+$ and $pp\rightarrow d\pi^+$ reactions. This is not too surprising since, for the $pp\rightarrow d\pi^+$ reaction, contributions from the terms $\mathrm{Im}(a_1a_2^*)$ and $\mathrm{Im}(a_2a_6^*)$ are both large and of opposite sign.

3. Contribution of P/D-class terms

The coefficients presented in Tables III and IV summarize the primary results of the present experiment for the $pp\rightarrow pn\pi^+$ reaction. Fortunately, additional information, while not at the individual amplitude level, but at the level of the contribution of the different transition classes, can be obtained. Because the momentum distribution functions fall into two main groups, as noted in connection with Figs. 1 and 2, with each group comprising a different set of the transition classes, the contribution of each to the cross section and analyzing powers can be assessed. However, since these groups of functions do not form an orthogonal set, the uncertainties in determining the contribution of each is much greater. This information was already contained in the earlier analysis and is now presented in Tables V and VI.

We first discuss the cross section results in Table V. Two columns appear under each of the headings P_0 and P_2, representing the further breakdown into different sets of transition classes. The coefficients $A_{\Gamma l}$ represent a limited sum over γ of the $A_{\gamma l}$. Thus the second column labeled $Ss+Sp+Sd$ represents contributions, expressed in terms of the amplitudes of Table I, from $|a_0|^2,|a_1|^2,|a_2|^2,|a_3|^2$, etc.; the fourth column labeled $Sp+Sd$ represents contributions from $|a_2|^2,\ldots|a_6|^2$, $\mathrm{Re}(a_0a_2^*)$, and $\mathrm{Re}(a_1a_3^*)$. Hence, the first column under each of the Legendre polynomial headings includes the transition classes where the pn orbital angular momentum state is $l_{pn}=0$. For convenience we will refer to these collectively as *S*-class transitions. The second column under each of the Legendre polynomial headings contains all the remaining terms for $l_{pn}=1,2$. Collectively these will be referred to as P/D-class transitions. Practically, the fitting was limited to $Pp+Pd+Dp$ in this category, as the table indicates. Furthermore, possible cross terms of the type

TABLE IV. Coefficients $B_l=\Sigma_\gamma B_{\gamma l}$ (μb) in the associated Legendre polynomial expansion P_l^1 of the analyzing power for the $pp\rightarrow pn\pi^+$ reaction.

	P_1^1	P_2^1	P_3^1	P_4^1	
420 MeV	-138.6 ± 3.0	14.8 ± 3.6	26.8 ± 1.5	-3.8 ± 1.2	[a]
	-143.1 ± 1.5	14.7 ± 1.3	21.6 ± 1.1	-3.1 ± 1.2	
	-84.3	23.7	56.2	2.1	$pp\rightarrow d\pi^+$
500 MeV	-259.2 ± 4.8	33.1 ± 3.8	172.0 ± 2.2	-3.3 ± 0.8	
	318.6	60.2	228.3	11.9	$pp\rightarrow d\pi^+$

[a] *S*-class only terms included in fit.

TABLE V. Coefficients $A_{\Gamma l}$ (μb) in the Legendre polynomial expansion P_l of the differential cross section for the $pp \rightarrow pn\pi^+$ reaction.

	P_0		P_2		
	$Ss+Sp+Sd$	$Pp+Pd+Dp$	$Sp+Sd$	$Pp+Pd+Dp$	
420 MeV	665±7		539±8		[a]
	673±10	10±15	576±38	38±57	
500 MeV	2027±26	239±19	1967±510	182±510	

[a] S-class only terms in this fit.

$SsDs$, $SsDd$, $SpDp$, $SdDs$, and $SdDd$ that appear in the expression for the cross section were not included in the fitting procedure. Doing so would have resulted in a function set that was much too large, leading to results that could not be interpreted. A meaningful division of the P_4 term into S-class and P/D-class terms could not be made. The first entry in Table V for 420 MeV shows a fit using S-class terms only. Comparing this result with the second entry that uses both S-class and P/D-class terms suggests that S-class terms alone are sufficient at this energy. On the other hand, at 500 MeV the P/D-class terms are important, although not very large, in the P_0 coefficient. Large uncertainties are associated with the two terms that make up the P_2 coefficient.

A similar division of the coefficients of the P_l^1 for the analyzing powers into groups involving S-class cross terms only, and those involving PP-class terms, are shown in the heading of Table VI. The first column under each of the P_l^1 represents the former terms. Specifically, a term like $SsSp$ would include a contribution from $\mathrm{Im}(a_1 a_2^*)$, while $PpPd$ would include a contribution from $\mathrm{Im}(c_2 c_5^*)$. The coefficients $B_{\Gamma l}$ thus represent a limited sum over γ of the $B_{\gamma l}$. The table shows that at 420 MeV the non-S-class terms are generally small, with significant uncertainties. This is consistent with the observation for the cross section that at 420 MeV S-class terms alone appear to be sufficient to describe the data. At 500 MeV the non-S-class terms are clearly important. Indeed, using S-class terms only resulted in a very poor fit to the analyzing power data.

D. Phenomenological description of the analyzing powers

A phenomenological interpretation of the earlier $pp \rightarrow pn\pi^+$ reaction study [7] made a prediction of the analyzing powers based on the analyzing powers of the $pp \rightarrow d\pi^+$ reaction. This prediction involved calculation of the $pp \rightarrow d\pi^+$ analyzing powers at the pion c.m. angle and pion momentum observed in the $pp \rightarrow pn\pi^+$ reaction. Analyzing powers calculated in this way were in good agreement with experiment. The equivalent formulation is obtained by a modification of the FSI calculation, Eq. (5), that now becomes

$$\frac{d^2\sigma}{d\Omega dx}(pp \rightarrow \{np\}\pi^+) = \frac{P(-1)}{P(x)} \frac{E(x)}{E(-1)} \frac{\sqrt{x}}{2\pi(x+1)} \frac{d\sigma}{d\Omega}(pp \rightarrow d\pi^+). \tag{8}$$

Here P and E are the c.m. incident proton momentum and energy. The two reactions are now evaluated at quite different c.m. energies, except when Q is small. This expression should be a good approximation, to the extent that the final pn state is $^3S_1$. Applying this expression to the calculation of the analyzing powers leads to the results shown by the dashed lines in Figs. 11 and 12. With the exception of the more forward angles the analyzing powers are surprisingly well represented by Eq. (8). Even for the forward angles there is good agreement in the vicinity of the highest pion momenta. This level of agreement emphasizes the close connection between the two-body and three-body final states.

E. Covariant one-boson-exchange model

In Sec. II a brief description was given of a covariant one-boson-exchange model [16,17]. Predictions from this model for the cross section distributions are shown in Figs. 9 and 10. All the parameters used in these calculations are the same as those given in Refs. [16,17]. The dashed lines represent the full calculations in which FSI effects are included; the dot-dash lines are calculations without the FSI effects. The laboratory angle information in these figures applies to the experimental data; the theoretical calculations were made at 5° intervals, i.e., 25°, 30°, etc. Most notable is the large

TABLE VI. Coefficients $B_{\Gamma l}$ (μb) in the associated Legendre polynomial expansion P_l^1 of the analyzing power for the $pp \rightarrow pn\pi^+$ reaction.

	P_1^1		P_2^1		P_3^1	
	$SsSp+SpSd$	$PpPd$	$SsSd+SdSd$	$PpPp$	$SpSd$	$PpPd$
420 MeV	−137±24	−7±11	20±18	−11±6	35±6	−14±6
500 MeV	122±85	−382±40	60±57	−79±13	188±7	−16±17

difference between the two calculations in the vicinity of the highest pion momenta. Without the FSI the calculations greatly underpredict the cross sections in this region. The general shape of the theoretical curves with the FSI follows the shape of experimental data very well over most of the momentum range. However, the experimental data have a stronger angular dependence; thus while the larger angles are fit rather well, at forward angles the data are quite a bit higher. The total cross sections given by this model are 0.681 and 2.532 mb for the energies of 420 and 500 MeV, respectively. This compares with the experimental values of 0.750 ± 0.075 and 2.77 ± 0.28 mb at these two energies, respectively.

VI. SUMMARY AND CONCLUSIONS

Differential cross sections and analyzing powers have been measured for the $pp\rightarrow pn\pi^+$ reaction over the pion angular range from 24° to 100° (lab) at 420 and 500 MeV. The inclusive measurements in this single arm experiment covered pion (lab) energies from the onset of the three body continuum to energies as low as 25 MeV. The total $pp\rightarrow pn\pi^+$ reaction cross sections extracted from the analysis were 0.750 ± 0.075 and 2.77 ± 0.28 mb at these two energies, respectively. These values include the contributions of both $T=0$ and $T=1$ final isospin states (i.e., σ_{10} and σ_{11}). Values for σ_{11} could not be separately ascertained, but were fixed at values of 69 and 502 μb, respectively, deduced from the $pp\rightarrow pp\pi^0$ reaction. The errors shown above are dominated by the overall normalization uncertainty of $\pm10\%$. A summary of the earlier data for the $pp\rightarrow pn\pi^+$ reaction is presented in Fig. 16 of Ref. [2]. The results from this experiment are consistent with these earlier data but have error bars which are much smaller. Calculations from the parametrization of VerWest and Arndt [32] (a curve for which is also shown in the above figure) lead to values of 0.82 and 2.44 mb, respectively, at these two energies. Predictions from the one-boson-exchange model (with FSI) [16,17] are 0.681 and 2.532 mb for these two energies, respectively. Both are a bit smaller but within 10% of the results of this experiment.

The coefficients A_0 and A_2 in the Legendre expansion of the differential cross section are well established from the present analysis, as shown in Table III. However, A_2 has a somewhat greater uncertainty because it is not independent of the value of the A_4 coefficient. The latter was not well established in this analysis. Also of note is the fact that the ratio A_2/A_0 is approximately unity for both the $pp\rightarrow pn\pi^+$ and $pp\rightarrow d\pi^+$ reactions for both of the energies. This is consistent with the dominance of the resonant a_2 amplitude.

Table IV shows that the coefficients B_l in the associated Legendre expansion of the analyzing powers are well established from the present analysis, with small uncertainties for the dominant terms.

An effort to further subdivide the coefficients A_l and B_l into S-class and non-S-class terms was presented in Tables V and VI. The evidence is not compelling that the latter terms are necessary at 420 MeV. However, they are essential at 500 MeV, where the analyzing powers in particular, could not be fit using S-class terms only. The internal np excitation energies can attain values as high as 50 and 85 MeV at the lowest measured pion energies, for bombarding energies of 420 and 500 MeV, respectively. Thus it is not surprising that there should be contributions from transitions involving $l_{pn}>0$. Perhaps surprising is the observation that such contributions appear to be so small at 420 MeV.

TABLE VII. Contribution to the $pp\rightarrow pn\pi^+$ cross section (μb) of the amplitudes a_1 and (a_0+a_2).

		Exp	Daehnick [a]	$pp\rightarrow d\pi^+$ [b]
420 MeV	a_1	193 ± 5	288	78
	a_0+a_2	471 ± 5	318	907
500 MeV	a_1	193 ± 14	650	55
	a_0+a_2	1831 ± 14	1092	1910

[a] Extrapolated from the low energy results of Daehnick [21].
[b] Calculated from the parametrization PPID [13].

The shapes of the pion momentum distribution functions are quite different for the Ss and Sp class transitions because of FSI effects, as shown in Fig. 1. Thus for this case alone it is possible to make some statement about the contributions to the cross section of the individual amplitudes a_1 and a_0+a_2. Table VII indicates these contributions as obtained from the analysis of Sec. V C. At energies from threshold to 330 MeV the contributions of these amplitudes has been presented by Daehnick [21]. A power law dependence of the square of these amplitudes is indicated; $|a_1|^2\propto\eta^{2.9}$ and $|a_2|^2\propto\eta^{4.4}$, with the same dependence for a_0 as for a_2. Extrapolating from these lower-energy data to the energies of 420 and 500 MeV results in the cross section contributions shown in the second last column of Table VII. The strong disagreement of these values with those from the present experiment indicates that such an extrapolation is not valid. Indeed, at these higher energies the magnitude of $|a_1|^2$ has leveled off, while $|a_2|^2$ is increasing at a rate more rapid than $\eta^{4.4}$. Simple phase space considerations [9] predict dependencies η^2 and η^4 compared with the values of 2.9 and 4.4. Table VII also gives the contributions of these amplitudes to the $pp\rightarrow d\pi^+$ reaction cross sections. For further comparison we note that the a_1 contribution to this reaction actually drops from 420 to 500 MeV, while for the $pp\rightarrow pn\pi^+$ reaction it remains constant. The a_1 amplitude contribution dominates the cross section in the $pp\rightarrow pn\pi^+$ reaction up to 330 MeV [21], decreasing to about 7% at 500 MeV.

The results presented in Tables V, VI and VII, and the related discussions, clearly depend on the momentum distribution functions (Figs. 1 and 2) that were used in the analysis. How the various conclusions would be modified with a different set of distribution functions is not easy to assess, short of a complete reanalysis using different input assumptions. Unfortunately, there are no other theoretical predictions for these distribution functions appropriate to this energy range. The above concerns do not apply to the results presented in Tables III and IV; the coefficients in these tables were quite insensitive to a range of fitting attempts where different constraints were imposed.

The predictions of the covariant one-boson-exchange model, with the inclusion of FSI effects, provide a very good fit to the experimental data, in general. However, the experimental data show a stronger angular dependence. Calculations from this model without FSI effects greatly underpredict the cross sections at the higher pion momentum values. Thus in this region of low relative pn energies FSI effects are very pronounced and must be included in any model of this reaction. Total cross section predictions of the CEOBEM model are somewhat lower, but within 10% of the current experiment.

In the present form of the CEOBEM model, the rescattering among the final particles is considered to be independent of the primary pion production process. Inherent therein is the assumption that the reaction takes place over a very small region of space, which is expected to be well fulfilled for reactions at low energies. Otherwise, the distortion of the final state will have to be calculated more precisely using the same interaction as that leading to pion production. Making these changes represents a major new theoretical undertaking.

The CEOBEM introduces some new elements in the phenomenological analysis of the present reaction as compared to earlier such models. It highlights the importance of performing the calculations in a fully covariant way which was lacking in the previous models [14,15,34–36]. It is possible to describe the production of both π^+ and π^0 in pp collisions near the kinematical threshold within one consistent picture within this model. At the same time, there is not unrestricted freedom to choose the parameters of the model so as to fit the pion data.

ACKNOWLEDGMENTS

Many fruitful exchanges with C. Wilkin and G. Fäldt are gratefully acknowledged. Thanks are also due to U. Mosel for useful discussions on the CEOBEM calculations. This work was supported in part by the Natural Sciences and Engineering Research Council of Canada.

---

[1] W.W. Daehnick, S.A. Dytman, J.G. Hardie, W.K. Brooks, R.W. Flammang, L. Bland, W.W. Jacobs, T. Rinckel, P.V. Pancella, J.D. Brown, and E. Jacobson, Phys. Rev. Lett. **74**, 2913 (1995).
[2] J.G. Hardie, S.A. Dytman, W.W. Daehnick, W.K. Brooks, R.W. Flammang, L.C. Bland, W.W. Jacobs, P.V. Pancella, T. Rinkel, J.D. Brown, and E. Jacobson, Phys. Rev. C **56**, 20 (1997).
[3] R.W. Flammang, W.W. Daehnick, S.A. Dytman, D.J. Tedeschi, R.A. Thompson, T. Vrana, C.C. Foster, J.G. Hardie, W.W. Jacobs, T. Rinckel, E.J. Stephenson, P.V. Pancella, and W.K. Brooks, Phys. Rev. C **58**, 916 (1998).
[4] J. Hudomalj-Gabitzsch *et al.*, Phys. Rev. C **18**, 2666 (1978).
[5] A.D. Hancock *et al.*, Phys. Rev. C **27**, 2742 (1983).
[6] C.E. Waltham *et al.*, Nucl. Phys. **A433**, 649 (1985); R.L. Shypit *et al.*, Phys. Rev. Lett. **60**, 901 (1988); T.S. Bhatia, *et al.*, Phys. Rev. C **28**, 2071 (1983); A.B. Wicklund *et al.*, Phys. Rev. D **35**, 2670 (1987).
[7] W.R. Falk, E.G. Auld, G. Giles, G. Jones, G.J. Lolos, W. Ziegler, and P.L. Walden, Phys. Rev. C **32**, 1972 (1985).
[8] A.H. Rosenfeld, Phys. Rev. **96**, 130 (1954).
[9] A.H. Rosenfeld, Phys. Rev. **96**, 139 (1954).
[10] M. Gell-Mann and K. Watson, Annu. Rev. Nucl. Sci. **4**, 219 (1954).
[11] L.G. Pondrom, Phys. Rev. **114**, 1623 (1959).
[12] Report No. 11-2, 1981, edited by J. Bystricky and F. Lehar (unpublished).
[13] W.R. Falk, Phys. Rev. C **50**, 1574 (1994).
[14] J. Dubach, W.M. Kloet, and R.R. Silbar, Nucl. Phys. **A466**, 573 (1987).
[15] A. Matsuyama and T.-S.H. Lee, Phys. Rev. C **34**, 1900 (1986).
[16] A. Engel, R. Shyam, U. Mosel, and A.K. Dutt-Mazumder, Nucl. Phys. **A603**, 387 (1996).
[17] R. Shyam and U. Mosel, Phys. Lett. B **426**, 1 (1998).
[18] K.M. Watson, Phys. Rev. **88**, 1163 (1952); A.B. Migdal, Sov. Phys. JETP **1**, 2 (1955).
[19] D.V. Bugg, A. Hasan, and R.L. Shypit, Nucl. Phys. **A477**, 546 (1988); D.V. Bugg, *ibid.* **A437**, 534 (1985); R.A. Arndt, I.I. Strakovsky, R.L. Workman, and D.V. Bugg, Phys. Rev. C **48**, 1926 (1993), and references therein.
[20] B. Blankleider and I.R. Afnan, Phys. Rev. C **31**, 1380 (1985).
[21] W.W. Daehnick, in Proceedings of the Seventh International Symposium on Meson-Nucleon Physics and the Structure of the Nucleon, Vancouver, B.C., Canada, 1997, edited by D. Drechsel, G. Höhler, W. Kluge, H. Leutwyler, B.M.K. Nefkens, and H.-M. Staudenmaier, TRIUMF Report No. TRI-97-1, 1997 (unpublished), p. 108.
[22] M.A. Preston, *Physics of the Nucleus* (Addison-Wesley, Reading, 1962).
[23] R. Abegg, W.P. Alford, D. Frekers, K. Hicks, R. Schubank, P. Walden, and S. Yen, TRIUMF internal report, 1985 (unpublished).
[24] M. Vetterli *et al.*, TRIUMF internal report, 1990 (unpublished).
[25] S. Yen, TRIUMF Report No. TRI-DN-88-10, 1988 (unpublished).
[26] P.L. Walden *et al.*, Nucl. Instrum. Methods Phys. Res. A **421**, 142 (1999).
[27] P.W. Green, TRIUMF Report No. TRI-DNA-91-1, 1991 (unpublished).
[28] K.L. Brown, F. Rothacker, D.C. Carey, and Ch. Iselin, Report No. SLAC-91, 1977 (unpublished).
[29] S. Yen, Nucl. Instrum. Methods Phys. Res. A **320**, 493 (1991).
[30] R.A. Arndt, Scattering analysis interactive dial-in program SAID (unpublished).
[31] A. Boudard, G. Fäldt, and C. Wilkin, Phys. Lett. B **389**, 440 (1996).
[32] B.J. VerWest and R.A. Arndt, Phys. Rev. C **25**, 1979 (1982).
[33] S. Stanislaus, D. Horvath, D.F. Measday, A.J. Noble, and M. Salomon, Phys. Rev. C **44**, 2287 (1991).
[34] M.E. Schillaci, R.R. Silbar, and J.E. Young, Phys. Rev. Lett. **21**, 711 (1968); Phys. Rev. **179**, 1539 (1969).
[35] T.-S.H. Lee and A. Matsuyama, Phys. Rev. C **36**, 1459 (1987).
[36] J. Dubach, W.M. Kloet, and R.R. Silbar, Phys. Rev. C **33**, 373 (1986).